Korean J. Chem. Eng., 40(1), 162-174 (2023)
DOI: 10.1007/s11814-022-1211-3

pISSN: 0256-1115
eISSN: 1975-7220

Species resolved interaction mechanism between graphene oxide and Cu(II) in aqueous solution with implications on wastewater remediation

Chaoke Bulin*,†, Ting Guo, Ruichao Zhao***,†, Rongxiang Zheng*, Bangwen Zhang****, and Fang Liu*****

*College of Materials and Metallurgy, Inner Mongolia University of Science and Technology, Baotou 014010, P. R. China
**College of Energy and Environment, Inner Mongolia University of Science and Technology, Baotou 014010, P. R. China
***Analysis and Testing Center, Inner Mongolia University of Science and Technology, Baotou 014010, P. R. China
****School of Materials and Metallurgy, Chongqing University of Science and Technology, Chongqing 401331, P. R. China
*****Inner Mongolia Jincai Mining Company Limited, Hohhot 010010, P. R. China
(*Received 4 May 2022 • Revised 13 June 2022 • Accepted 19 June 2022*)

Abstract−Heavy metals discharged into water by industrial activity give rise to severe environmental pollution. Herein, graphene oxide (GO) was prepared based on an improved Hummers method and utilized as adsorbent to remove aqueous Cu(II). The "species resolved" adsorption mechanism was deeply inspected via combining multiple explorations extracted from Cu(II) species distribution, GO surface charge, adsorption experiment and fitting, hard-soft acid-base (HSAB) theory, FTIR and XPS spectra. Different adsorption mechanism resolved by Cu(II) species was proposed, corresponding to different pH range. (1) When pH<8, bare Cu^{2+} is the dominant Cu(II) species, ion exchange and chemical complexation are the adsorption mechanism. (2) When pH=8, $Cu(OH)_2$ is the dominant Cu(II) species, precipitation, ion exchange and chemical complexation are the adsorption mechanism. (3) When pH>8, $Cu(OH)_3^-$ is the dominant Cu(II) species, electrostatic attraction is the adsorption mechanism. Electron transfer and energy lowering calculated based on the HSAB theory demonstrates, OH is stronger than COOH regarding binding affinity towards Cu(II). As for adsorption efficiency, adsorption of Cu(II) onto GO equilibrated in 12 min, with adsorption percent and quantity 92.32% and 553.90 $mg \cdot g^{-1}$, respectively. Findings of this work may shed light on the interaction mechanism of graphene oxide with heavy metals. Accordingly, these as clarified mechanisms may provide guidance for developing efficient adsorbent based on graphene for heavy metal scavenging.

Keywords: Graphene Oxide, Cu(II), HSAB Theory, Species Resolved, Interaction Mechanism

INTRODUCTION

Highly toxic heavy metals discharged into water by industries, including battery, mining, metallurgy, electroplating, ceramics [1], give rise to severe environmental pollution, which has brought unprecedented threat and challenge towards human survival and development. Therefore, developing techniques for efficient harnessing heavy metal pollution is both academically interesting and practically challenging.

Heavy metals are chemically stable and refractory, thereby can hardly be effectively remediated by degradation techniques as proven to be effective in handling organic or biological contaminants such as dyes, pesticides, and viruses. Common techniques for heavy metal remediation include ion exchange [2], chemical sediment [3], membrane separation [4], coagulation [5], and adsorption [6]. Among these, adsorption is the most attractive and promising, due to its tailorable design, low cost, and easy operation. A diversity of adsorbents, including activated carbon [7], clay [8], resin [9], MOF [10], as well as carbonaceous materials including carbon nanotube [11] and graphene [12], were extensively investigated for heavy metal sequestering, and promising application potential was proposed. However, they suffer from defective efficiency, selectivity, and recyclability. Further exploration of high performance adsorbent is summoning more research efforts.

Graphene oxide (GO) is an important graphene derivative, bears the same framework as pure graphene. Accordingly, GO inherits the basic characters of graphene such as high specific surface area and chemical stability. Moreover, GO has various oxygenous groups such as carbonyl, hydroxyl, carboxyl, epoxy, and phenol, which are absent in pure graphene. These groups have binding affinity towards heavy metals and other various contaminants, thus serve as adsorption sites. Therefore, GO based materials as potential high performance adsorbents towards aqueous heavy metal have become a research hotspot [12,15,21,24,27,30-36], mainly focusing on the removal performance and interaction mechanism.

With regard to the synthetic method of GO, the famous Hummers method [13] is the most widely employed one. By the strategy of this method, graphite layers are exfoliated and oxidized nearly simultaneously by oxidants $KMnO_4$ and concentrated H_2SO_4, thus the above mentioned oxygenous groups are introduced to form GO colloidal. Accordingly, the species, quantity, and distribution of the oxygenous groups which determine the adsorption capability, depend highly on GO synthesis condition.

To develop a more economical and efficient method for GO syn-

†To whom correspondence should be addressed.
E-mail: quan820720@126.com, wszrc7@126.com
Copyright by The Korean Institute of Chemical Engineers.

thesis, our group [14] made some improvements on the conventional Hummers method: (1) Removed $NaNO_3$ which emits toxic NO_2 and N_2O_4. (2) Replaced partial $KMnO_4$ by K_2FeO_4. (3) Reduced the dosage of concentrated H_2SO_4. Based on the improved method, GO was synthesized efficiently, subsequently a series of graphene based materials were fabricated using GO as precursor. These graphene based materials were employed as adsorbents for various aqueous contaminants, including heavy metals and dyes [15,16].

Revealing the adsorption mechanism from the aspect of adsorbent-adsorbate interaction can provide enlightening guidance for designing high performance adsorbent at an atomic level. Therefore, clearly elucidating the interaction mechanism between the "exact" adsorbent and adsorbate who do interact in the ad hoc adsorption system is essential. Regrettably, the surface properties of adsorbent and species distribution of adsorbate are quite elusive as to highly dependent on the aqueous environment. They evolve sensitively with the variation of important aqueous parameters like pH. To the authors' knowledge, there is little information about literature on the discussion about this kind of interaction mechanism, which might as well be called "species resolved" mechanism.

In this work, GO was prepared based on the Hummers method improved by our group. Aqueous Cu(II) was adopted as a model pollutant to test the removal capability of GO as potential adsorbent via batch adsorption experiments. For unravelling the "species resolved" mechanism, the quantitative evolution of aqueous Cu(II) species, as well as variation of the surface charge of GO with pH was taken into consideration. More critically, the hard-soft acid-base (HSAB) theory was adopted to elucidate the interaction mechanism in a quantitative level. Specifically, the interaction intensity was evaluated by energy lowering and charge transfer as calculated within the framework of HSAB theory.

The hard-soft acid-base (HSAB) principle was proposed by Pearson [17] to predict the chemical reactivity between Lewis acids and bases qualitatively. Thereafter, Pearson [18] developed a standard via defining a parameter called "absolute hardness" to evaluate the chemical reactivity quantitatively. As different functional groups in GO have different adsorption affinities towards a certain contaminant, the author believes that the HSAB theory which has a wide sphere of applicability can bring useful enlightenment on the interaction mechanism between GO and heavy metal.

MATERIALS AND METHODS

1. Material Preparation

All reagents purchased from Beijing Chemical Reagent Co, China were of analytical purity and used without further purification. The detailed procedure of GO preparation is described in our previous publication [14], briefly as follows. Natural flake graphite (10 g), $KMnO_4$ (6 g), K_2FeO_4 (4 g) and H_3BO_3 (0.1 g) were added into a reaction flask containing H_2SO_4 (98 wt%, 100 mL), and stirred for 1.5 h in an ice bath. Then, an extra amount of $KMnO_4$ (5 g) was added and the reaction flask transferred into a water bath at 35 °C, followed by 3 h stirring. Subsequently, the temperature was raised to 95 °C and kept until the reaction mixture turned brown. Afterwards, H_2O_2 (30 wt%, 12 mL) was dropwise added. Finally, the reaction mixture was cleansed with dilute HCl solution and deionized water several times to obtain the GO suspension.

2. Characterization Methods

The crystalline state of the sample was characterized by X-ray diffractometer (XRD; PANalytical X'Pert PRO, Netherlands). Sample morphology was surveyed using transmission electron microscopy (TEM; JEOL JEM-2100, Japan). The sample thickness was investigated using atomic force microscope (AFM; Dimension Icon Bruker, Germany). The functional groups of the samples were analyzed by Raman spectra (RS; XploRA PLUS, France), ultraviolet-visible spectroscopy (UV-Vis; HITACHI U-3900, Japan) and Fourier transformation infrared spectroscopy (FTIR; Bruker, IFS66V, Germany). The surface elements of the samples were characterized using X-ray photoelectron spectra (XPS; Kratos Axis Supra, England). The thermal stability of the sample was assessed by thermogravimetry-differential thermal analysis (TG-DTA; NETZSCH, STA449C, Germany), whereby the weight content of the functional groups was determined. The surface area and porosity of the sample were tested by N_2 adsorption-desorption instrument (Micromeritics, ASAP 2020 V3.04 G, USA). The surface potential of the sample colloidal was measured using micro-electrophoresis meter (zeta potential; Shanghai Zhongchen Co. Ltd JS94H, China).

3. Batch Adsorption

The Cu(II) stock solution was prepared by dissolving $CuSO_4 \cdot 5H_2O$ in deionized water. For batch adsorption, the solution pH was adjusted to a target value using dilute HCl or NaOH solution with a concentration of approximately 0.1 $mol \cdot L^{-1}$, then the adsorbent was added. Immediately after the adsorbent addition, the test flask was shaken in an oscillator at a constant temperature to onset adsorption under an enhanced kinetic condition. After a certain duration, adsorbent was readily recovered via suction filtration. The filtered solution was tested for the residual concentration of Cu(II) by atomic absorption spectrophotometer (PerkinElmer A800, USA) to quantify the adsorption indices. These indices include the adsorbent dosage D ($mg \cdot L^{-1}$), adsorption percent R_i (%) and adsorption quantity Q_i ($mg \cdot g^{-1}$), which are determined by Eqs. (1)-(3):

$$D = \frac{m}{V} \tag{1}$$

$$R_i = \frac{C_0 - C_t}{C_0} \times 100\% \tag{2}$$

$$Q_i = \frac{(C_0 - C_t)V}{m} \tag{3}$$

The subscript i has three different implications concerning adsorption process: i=0, e, t, implies the start, equilibrium and any moment t, respectively. C_i ($mg \cdot L^{-1}$) and V (mL) are the concentration and volume of Cu(II) solution, m (g) is the adsorbent mass. All Q_i and C_i in this paper have the same implications as their counterparts in Eqs. (2)-(3).

4. Quantitative Evolution of Cu(II) Species with pH

The deduction process of the equation quantifying the Cu(II) species under a certain pH, as well as the species distribution curve was detailed in our previous report [15].

5. Adsorption Fitting

Isothermal fitting was implemented to explore the adsorption features, including adsorption type (homogeneous or heterogeneous

Table 1. HSAB theory related parameters regarding adsorption in this work

Adsorbate	Adsorbent	Adsorbate X_A	Adsorbate η_A	Adsorbent X_B	Adsorbent η_B	ΔN	ΔE
Cu^{2+}	Ar-COOH	28.56	8.27	4.90	4.80	0.91	−10.71
Cu^{2+}	Ar-OH	28.56	8.27	3.80	4.80	0.95	−11.73

adsorption) and interaction nature (physical or chemical interaction). Kinetic fitting was performed to inspect the process character (consecutive steps, and the rate limiting one involved in adsorption). The van't Hoff equation was employed to determine the thermodynamic parameters.

6. Analysis of Adsorbate-adsorbent Interaction Based on the Hard-soft Acid-base (HSAB) Theory

Within the framework of Lewis acids and bases, acid and base are defined as the electron acceptor and donator, respectively. The HSAB theory further developed the Lewis acids and bases conception. Herein, adsorbate and adsorbent are regarded as acid and base, respectively, to incorporate the HSAB theory [17] for inspecting the adsorbate-adsorbent interaction. Thereby, the electron transfer ΔN and energy lowering ΔE relating to adsorption are determined by Eq. (4) and Eq. (5), respectively [18]:

$$\Delta N = \frac{(X_A - X_B)}{2(\eta_A + \eta_B)} \quad (4)$$

$$\Delta E = \frac{(X_A - X_B)^2}{4(\eta_A + \eta_B)} \quad (5)$$

where the subscripts A and B symbolize acid and base, respectively. Accordingly, X_A, X_B denote the absolute electronegativity, η_A, η_B the absolute hardness of acid and base, respectively. All parameters in Eqs. (4)-(5) are quantified with eV as unit.

For discussing the adsorbate-adsorbent interaction, carboxyl COOH and hydroxyl OH were selected as representative groups of GO. Definitely, the adsorbate, adsorbent and adsorption are parallel to the role of acid, base and acid-base neutralization reaction, respectively, by their chemical connotation. Table 1 lists the values of absolute electronegativity and absolute hardness [19] of the chemical entities (i.e., interacting parts of adsorbent and adsorbate) involved in the adsorption, as well as the calculation results of ΔN and ΔE. Meanwhile, ΔN and ΔE are also graphically presented as Fig. 1.

Ar symbolizes the aromatic ring. Thereby, Ar-COOH and Ar-OH denote the carboxyl and hydroxyl groups in GO, respectively.

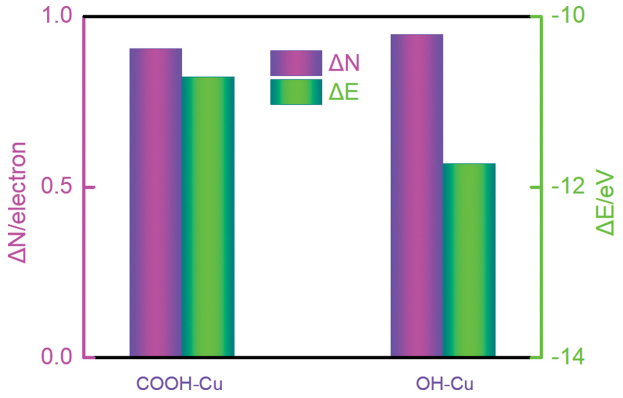


Fig. 1. Charge transfer (ΔN) and energy lowering (ΔE) regarding the interaction of groups COOH-, OH- in GO with Cu(II) as calculated using the HSAB theory.

RESULTS AND DISCUSSIONS

1. Characterization

Fig. 2 shows the XRD patterns of natural flake graphite and GO. For graphite, the prominent peak at 2θ=26.43° is the characteristic (002) diffraction [20]. For GO, a clear peak at 2θ=10.64° is attributed to the (001) diffraction of graphene oxide [21]. The peak intensity of graphene oxide is noticeably lower than that of graphite, indicating far inferior crystallinity of the former than the latter. The inferior crystallinity is due to the destruction of the long-range order of carbon atoms caused by oxidative exfoliation that intro-

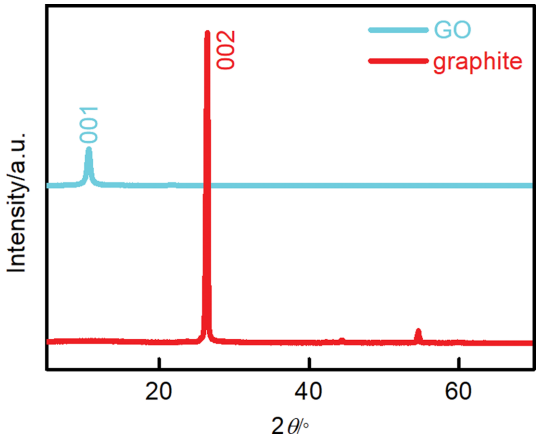


Fig. 2. XRD patterns of natural flake graphite and GO.

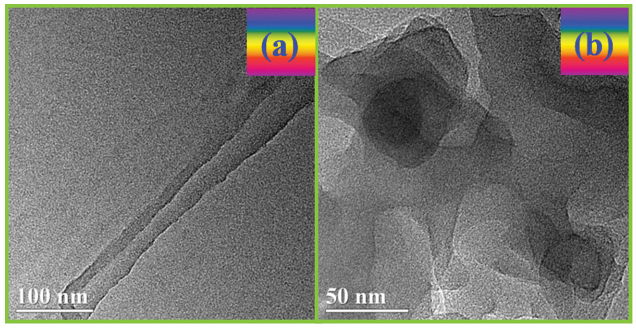


Fig. 3. TEM images of GO.

duced crystal defects.

The TEM images of GO as displayed by Fig. 3 reveal typical morphological features of graphene. Fig. 3(a) clearly exhibits the edges of three adjacent graphene sheets appear as three slashes parallel to each other. Fig. 3(b) clearly shows the boundaries of several graphene sheets appear as curvy lines. Besides, two pores appear at the upper left corner and lower right corner of the image. Evidently, distribution by random orientation makes graphene sheets interlaced, giving rise to these pores.

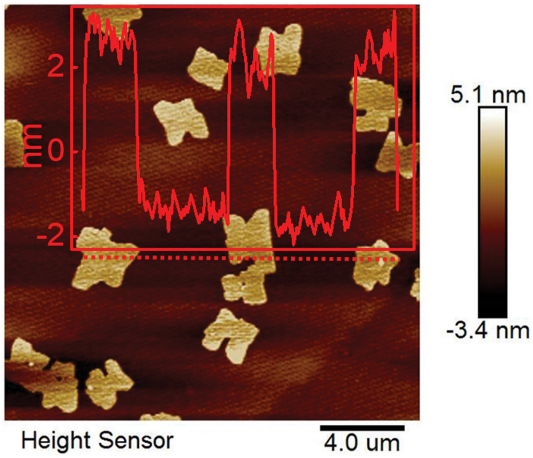


Fig. 4. AFM image and height profile of GO.

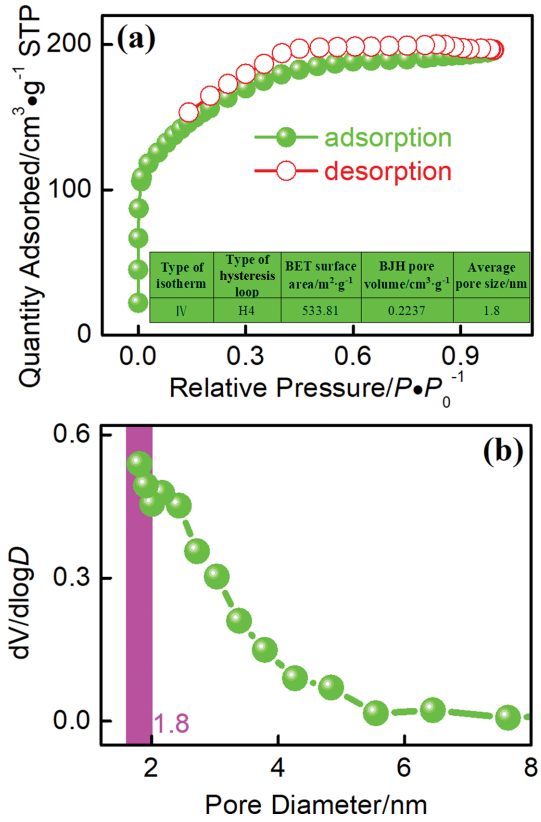


Fig. 5. N_2 adsorption-desorption isotherms (a) and pore size distribution (b) of GO.

The AFM image of GO in Fig. 4 illustrates graphene sheets, displaying the typical lamellar morphology. Moreover, the height profile revealing the thickness distribution of the sample along the dotted line demonstrates that the thickness of GO is less than 3 nm.

Fig. 5 displays the N_2 adsorption-desorption isotherms and pore size distribution curve of GO. Dramatic adsorption under low relative pressure, as well as subsequent adsorption plateau was observed. According to the IUPAC categorization, the isotherms and hysteresis loop are designated as type IV and H4, respectively, revealing slit shaped mesopores. Undoubtedly, these slit shaped pores stem from the intervals of the graphene sheets. The pore size was concentrated around 1.8 nm, verifying mesoporous character. More quantitatively, the BET surface area and BJH pore volume were 533.81 $m^2 \cdot g^{-1}$ and 0.2237 $cm^3 \cdot g^{-1}$, respectively. Evidently, such a high surface area is directly related to the thin morphology of GO as confirmed by AFM observation (Fig. 4). High surface area provides ample two-dimensional areas to accommodate adsorption sites. While considerable pore volume provides sufficient three dimensional space to arrange migration pathways. Accordingly, ameliorated conditions for adsorption thermodynamics and kinetics were created, respectively.

Fig. 6 shows the Raman spectrum of GO. The typical D band and G band characterizing the sp^3 and sp^2 carbon appear at 1,333 cm^{-1} and 1,585 cm^{-1} [22]. Definitely, sp^3 and sp^2 carbon reflects the magnitude of disorder and order in graphene based materials, respectively. More quantitatively, the intensity ratio I_D/I_G is 1.23, indicating that considerable portion of the inherent sp^2 carbon atoms was transformed into sp^3 ones bonded to oxygenous groups, thereby disorder was formed during GO preparation.

Fig. 7 displays the TG-DTA curves of GO. The whole thermal process comprises four consecutive stages, as highlighted by different background colors. The first stage, T<100 °C, the small weight loss of 0.45% stems from the volatilization of the surface water. The second stage, 100 °C<T<350 °C, prominent weight loss of 62.8% is due to the dissociation of the unstable oxygenous groups [23]. The third stage, 350 °C<T<448 °C, weight loss 7.6% is attributed to the decomposition of the robust oxygenous groups; the concomitant soaring temperature difference proved the firm bonding of these

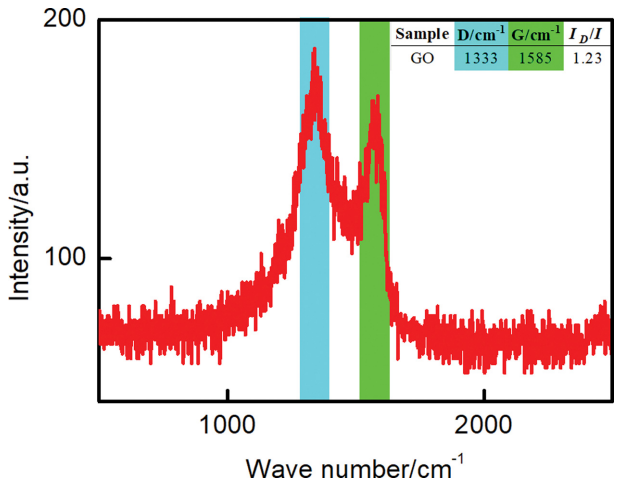


Fig. 6. Raman spectrum of GO.

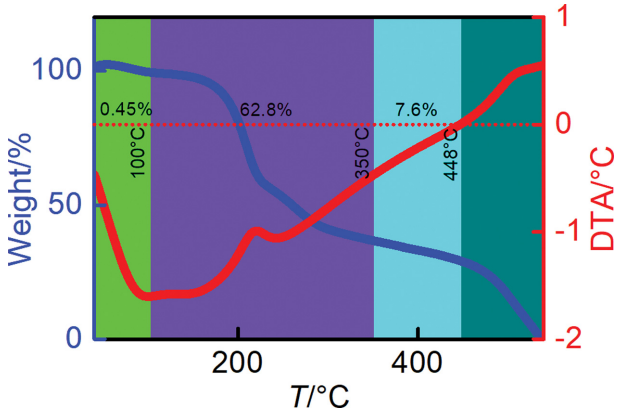


Fig. 7. TG-DTA curves of GO.

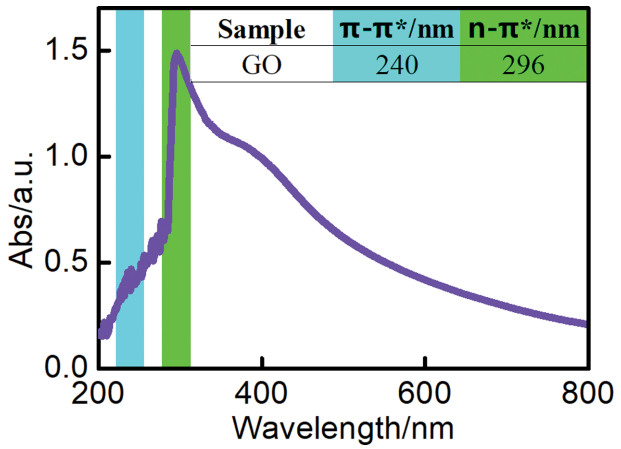


Fig. 8. UV-Vis spectrum of GO.

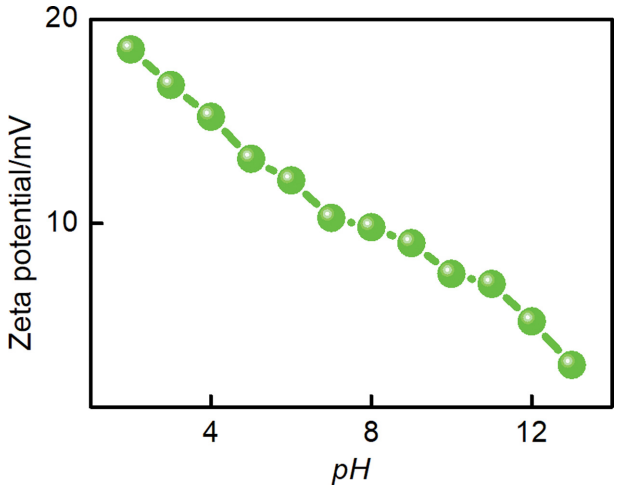
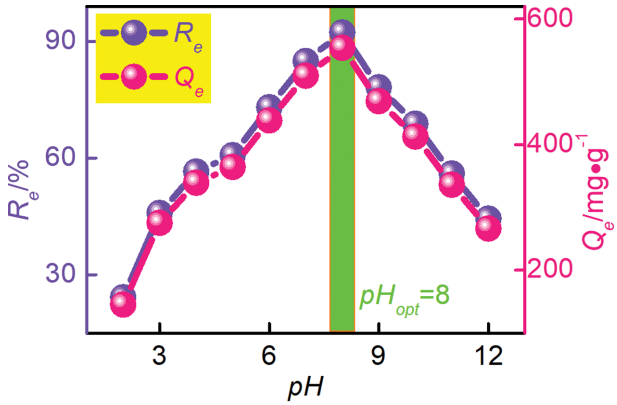


Fig. 9. Zeta potential of GO hydrosol under varying pH.



***pH* = 2-12**, t = 30 min, D = 500 mg·L^{-1}, C_0 = 300 mg·L^{-1}, T = 25 °C

Fig. 10. Effect of pH on the adsorption of Cu(II) by GO.

oxygenous groups onto graphene ring. The overall weight loss relevant to the oxygenous groups was noticeable, substantiating the considerable amount of oxygenous groups as concluded from the Raman spectrum. The fourth stage, T>448 °C, further weight loss and the continuously increasing temperature difference demonstrate the pyrolysis of the carbon framework.

The UV-Vis spectrum of GO in Fig. 8 presents two characteristic absorption peaks [24]. Particularly, the π-π* peak signifies the transition of conjugated electrons from the bonding orbital to the anti-bonding one. While the n-π* peak signifies the transition of lone pair electrons in the hetero atoms (O, N, S, etc.) to the anti-bonding orbital. The rather prominent n-π* peak implies the considerable magnitude of the hetero atoms relating to the functional groups in GO. This exploration is consistent with those derived from the Raman and TG-DTA analyses.

Fig. 9 shows the zeta potential of GO colloidal as a function of pH. Positive values were measured in the whole pH range 2-13, indicating electrostatic repulsion among graphene sheets. This repulsion hinders the stacking of graphene sheets as to make them disperse homogeneously.

2. Adsorption Experiments

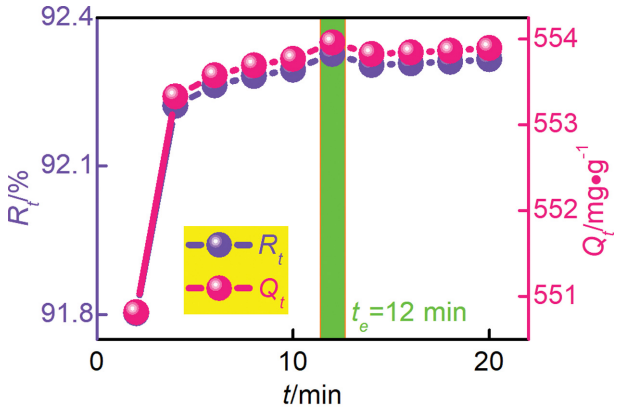
2-1. Effect of pH

pH is a key influential factor on adsorption needing careful inspection. For analyzing the pH effect on adsorption, as well as the adsorbent-adsorbate interaction using the HSAB principle, we chose carboxyl (COOH) and hydroxyl (OH) as models to represent the functional groups of GO. Fig. 10 presents, Cu(II) adsorption increases notably to reach its peak at pH=8. Accordingly, 8 was adopted as the optimal pH in all the subsequent assays. However, Cu(II) adsorption decreased drastically as pH increased further. We incorporated the species distribution of Cu(II), zeta potential of GO hydrosol shown in Fig. 9 and the HSAB theory related parameters regarding adsorption as listed in Table 1 to elucidate Fig. 10. When pH<8, the bare Cu^{2+} is the dominant Cu(II) species [15]. When pH=8, the pH under which adsorption is optimized, $Cu(OH)_2$ is the dominant species (with a molar fraction 0.8117). As pH increases in the range of 2-8, positive zeta potential of GO decreases (Fig. 9), leading to the weakening of the electrostatic repulsion between Cu^{2+} and GO. Accordingly, adsorption increase in the same pH range of 2-8 renders two explorations. (1) Weakening of electrostatic repulsion facilitated adsorption as to be optimized at pH=8. (2) Chemical interaction between Cu(II) (Cu^{2+}, $Cu(OH)_2$) and GO is strong enough to prevail over the electrostatic repulsion which serves as kinetic resistance against adsorption. However, when pH

exceeds 8, anions with high complexation grade such as $Cu(OH)_3^-$, $Cu(OH)_4^{2-}$ successively appear as the dominant species. In $Cu(OH)_3^-$ and $Cu(OH)_4^{2-}$, Cu(II) was complexed with more than three OH^-, resulting in three consequences. (1) As more than three bonding orbitals of Cu(II) were occupied by OH^- complexation, the reactivity, or affinity of Cu(II) with other chemical units including functional groups in GO is undermined. (2) More than three OH^- take up a large portion of the space surrounding Cu(II), serving as steric hindrance against the approaching of chemical units including functional groups in GO towards Cu(II). (3) Since the chemical complexation of Cu(II) with adsorption sites is notably restricted, electrostatic attraction between negative $Cu(OH)_3^-$ or $Cu(OH)_4^{2-}$ and positive GO may serve as the dominant adsorption mechanism. However, adsorption decrease under pH>8 proposes that electrostatic attraction as a form of adsorbent-adsorbate interaction is far weaker in strength than chemical complexation.

2-2. Effect of Contact Time

Contact time is an non-negligible adsorption factor, as it determines the adsorption efficiency to a great extent. Fig. 11 depicts that rapid Cu(II) adsorption occurred at the initial stage, as to reach equilibrium at 12 min (denoted as t_e=12 min in Fig. 11). Only minor fluctuations in adsorption were measured afterwards. Adsorption percent and quantity were 92.32% and 553.90 $mg \cdot g^{-1}$, respectively, under equilibrium. This high adsorption efficiency can be understood from the aspects of both thermodynamics and kinetics. (1) Thermodynamic aspect: Abundant oxygenous groups of GO provide sufficient adsorption sites for Cu(II). (2) Kinetic aspect: High specific surface area and considerable pore volume accommodate plentiful migration pathways for Cu(II).



pH = 8, ***t* = 2-20 min**, *D* = 500 mg·L^{-1}, C_0 = 300 mg·L^{-1}, *T* = 25 °C

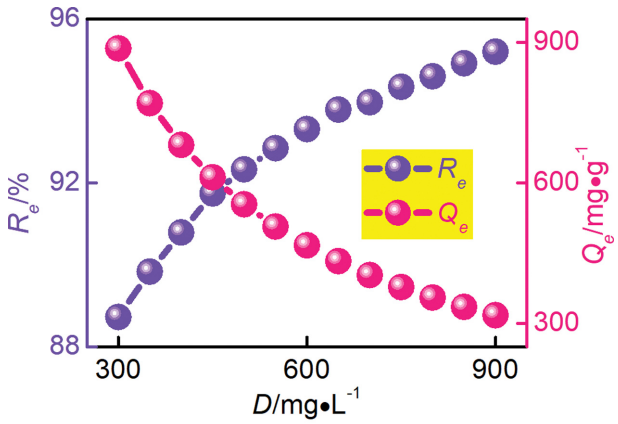
Fig. 11. Effect of contact time on the adsorption of Cu(II) by GO.

2-3. Effect of Adsorbent Dosage

Adsorbent dosage must be taken into consideration, as it is associated with the cost effectiveness of the adsorption work. Fig. 12 presents that adsorption percent increases while adsorption quantity decreases with increasing adsorbent dosage. Increasing dosage means more vacant adsorption sites, resulting in increasing adsorption percent. Whereas, when excessive adsorbent is added, nearly all the adsorbates will be adsorbed. More importantly, adsorbent particles may come close to each other and start to agglomerate under high dosage. Agglomeration deteriorates dispersion and makes some adsorption sites be wrapped inside, leading to lower adsorption quantity. The two adsorption indices can be reconciled under the adsorbent dosage of 500 $mg \cdot L^{-1}$ as to give a satisfactory performance: adsorption percent and quantity for Cu(II) are 92.32% and 553.90 $mg \cdot g^{-1}$.

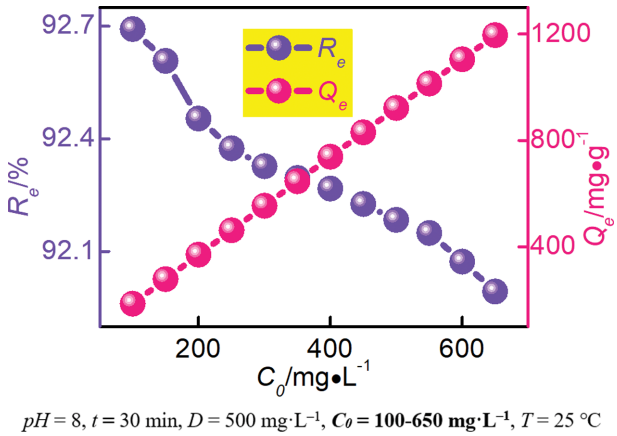
2-4. Effect of Adsorbate Initial Concentration

Real wastewater may have heavy metals with various concentrations. In consideration of the this case, adsorption efficiency of GO on Cu(II) with initial concentration 100-650 $mg \cdot L^{-1}$ was inspected to assess the concentration adaptability of GO. Fig. 13 depicts that adsorption percent decreases, while adsorption quantity increases as adsorbate initial concentration increase. First, nearly all the available adsorption sites become occupied under high adsorbate initial concentration, resulting in adsorption percent decrease (thermodynamic effect). Second, high adsorbate initial concentration enables high concentration gradient and more collision opportunity with adsorbent, resulting in adsorption quantity increase (kinetic effect). Overall, GO keeps adsorption percent higher than 92% on Cu(II) in the concentration range 100-650 $mg \cdot L^{-1}$, demonstrating good concentration adaptability.



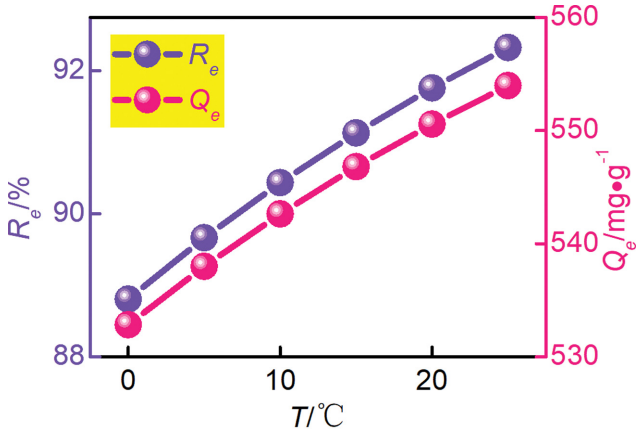
pH = 8, *t* = 30 min, ***D* = 300-900 mg·L^{-1}**, C_0 = 300 mg·L^{-1}, *T* = 25 °C

Fig. 12. Effect of GO dosage on the adsorption of Cu(II).



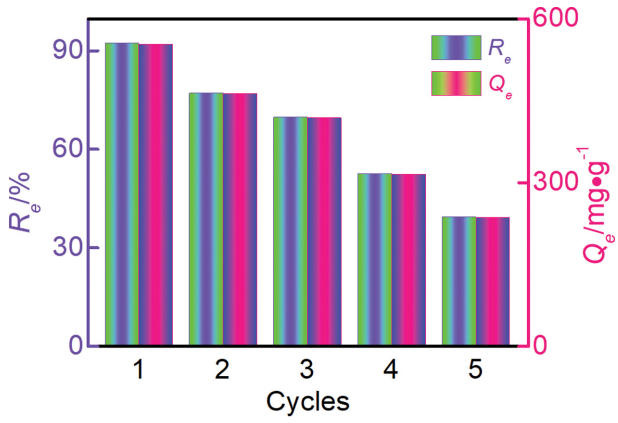
pH = 8, *t* = 30 min, *D* = 500 mg·L^{-1}, ***C*$_0$ = 100-650 mg·L^{-1}**, *T* = 25 °C

Fig. 13. Effect of Cu(II) initial concentration on its adsorption by GO.



$pH = 8$, $t = 30$ min, $D = 500$ mg·L^{-1}, $C_0 = 300$ mg·L^{-1}, T = **0-25 °C**

Fig. 14. Effect of temperature on the adsorption of Cu(II) by GO.



$pH = 8$, $t = 30$ min, $D = 500$ mg·L^{-1}, $C_0 = 300$ mg·L^{-1}, $T = 25$ °C, **cycles = 1-5**

Fig. 15. Cyclic adsorption efficiency of GO on Cu(II).

2-5. Effect of Temperature

Batch adsorption was conducted under temperature in the range of 0-25 °C to check the temperature effect. Fig. 14 displays adsorption efficiency improvement due to temperature increase. This indicates that adsorption is thermodynamically endothermic. Adsorption improvement can be rationalized from the perspective of thermodynamics and kinetics. The generally endothermic ionization of oxygenous groups in GO is facilitated by temperature increase to release more adsorption sites (thermodynamic perspective). The diffusion of adsorbates towards adsorbent is promoted by the enhanced Brownian motion due to temperature escalation (kinetic perspective).

2-6. Cyclic Adsorption Efficiency

Recycling efficiency of adsorbent is an important parameter that should be taken into consideration when put towards industrial application. In Fig. 15 after five consecutive cycles, GO kept adsorption quantity of 236.17 mg·g^{-1}, which is 43% of its original capacity. Generally, efficiency decay arises from parts of the adsorbent that fail to be recovered, and parts of the adsorption sites that fail to be generated. First, as being highly hydrophilic, GO can hardly be recovered completely. Second, as functional groups in GO have

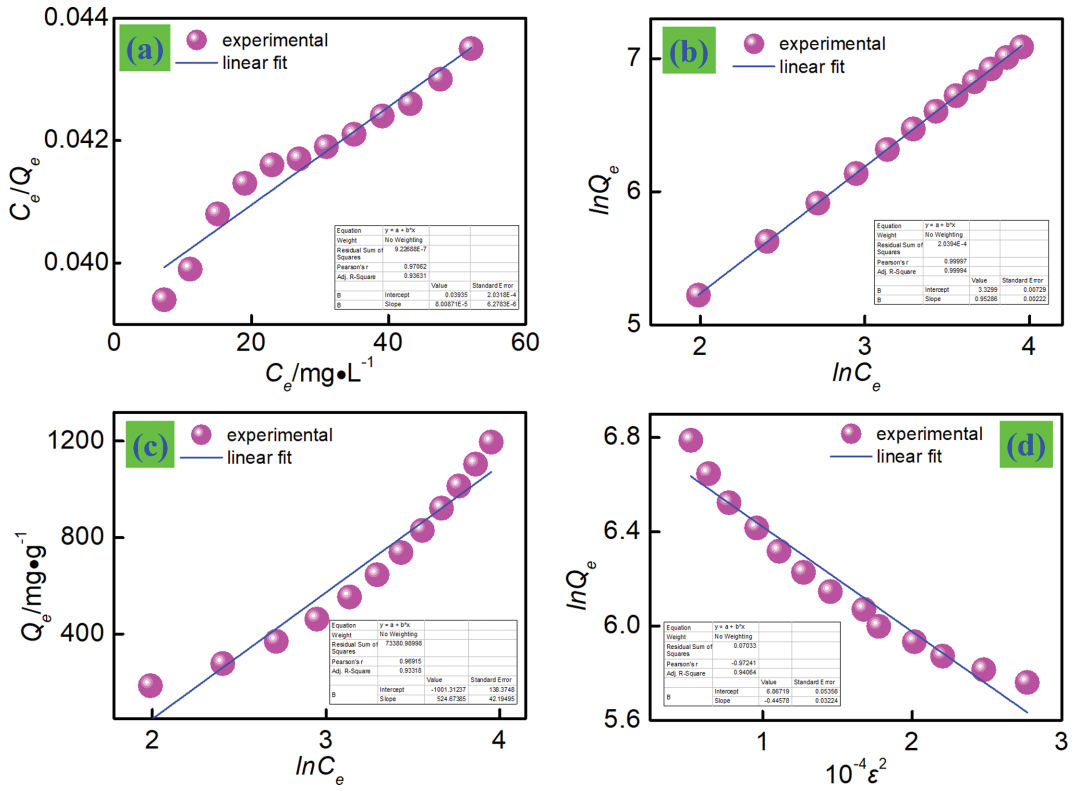


Fig. 16. Fitting curves of the adsorption of Cu(II) by GO based on various isotherm models: (a) Langmuir; (b) Freundlich, (c) Temkin, (d) D-R.

strong binding affinity towards heavy metal, these groups serving as adsorption sites can hardly be regenerated thoroughly. The non-negligible efficiency decay reminds us that further modification on GO is necessary to achieve satisfactory comprehensive performance to meet the need of practical application.

2-7. Adsorption Fittings

The connotations of the models (isotherms, kinetics, thermodynamics models) employed for adsorption fittings in this work were specified in our previous work [15,16]. Accordingly, definitions regarding model parameters are elaborated in the nomenclature section at the end of this article. The fitting results are presented both graphically (Fig. 16-18) and numerically (Table 2).

With respect to the four isotherm models, the Freundlich model yields the most satisfactory fitting as to give the highest correlation coefficient R^2 0.9985. Besides, the n parameter within the framework of Freundlich model disclosing adsorption type (chemical if n<1, physical if n>1) [25] is 0.8228. These results suggest: (1) GO surface is uneven with respect to adsorption activity, resulting in heterogeneous adsorption. Evidently, diversified functional groups in GO are the origin of this unevenness. (2) Adsorption type is primarily chemical. Moreover, the fitting result of the Temkin model was also rather satisfactory as to give high R^2 of 0.9748, further suggesting the chemical type of the adsorption [26]. However, fitting results of other isotherm models were less satisfactory.

Regarding the six kinetic models, the pseudo-second-order (PSO) model provides the most satisfactory fitting, giving the highest R^2 0.9999. More convincingly, adsorption quantity derived from PSO fitting is 555.56 $mg \cdot g^{-1}$, which matches the batch adsorption result 553.90 $mg \cdot g^{-1}$ (Fig. 11) quite satisfactorily. These explorations disclose that chemical interaction is involved in adsorption as a rate-

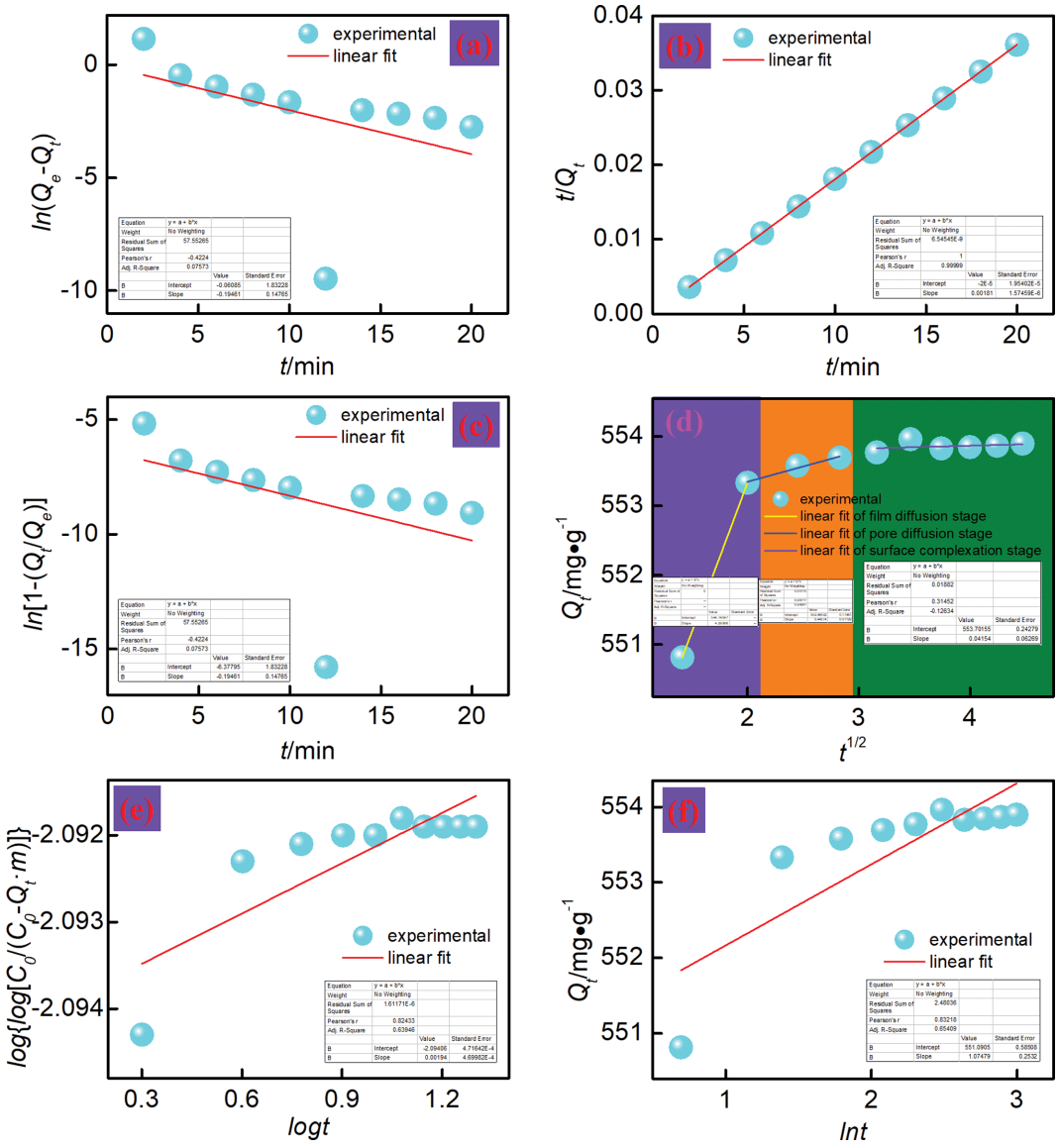


Fig. 17. Fitting curves of the adsorption of Cu(II) by GO based on various kinetic models (a) Pseudo-first order, (b) Pseudo-second order, (c) Liquid film diffusion, (d)-1, 2 Intra-particle diffusion of Cd(II), Cu(II) (external diffusion, internal diffusion, surface reaction), (e) Bangham, (f) Elovich.

Table 2. Fitting and calculation results of Cu(II) adsorption by GO

Types	Models	Formula	Parameters			R^2
Isotherm	Langmuir	$C_e/Q_e=1/(K_LQ_{max})+C_e/Q_{max}$	Q_{max}/mg·g^{-1} 12,486.4054	K_L/L·mg^{-1} 0.0020	R_L 0.4305-0.8309	0.9363
	Freundlich	$\ln Q_e=\ln K_F+(1/n)\ln C_e$	n 0.8228		K_F 12.1866	0.9985
	Temkin	$Q_e=(RT/A_T)(\ln B_T+\ln C_e)$	A_T/J·mol^{-1} 3.8043		B_T/L·g^{-1} 0.1056	0.9748
	D-R	$\ln Q_e=\ln Q_{max}-\beta\varepsilon^2$ $\varepsilon=RT\ln[1+(1/C_e)]$ $E=(2\beta)^{-0.5}$	Q_{max}/mg·g^{-1} 960.2465		E/J·mol^{-1} 105.9075	0.9406
Kinetics	Pseudo-first order	$\ln(Q_e-Q_t)=\ln Q_e-k_1t$	k_1/min^{-1} 0.1946		Q_e/mg·g^{-1} 0.9410	0.0757
	Pseudo-second order	$t/Q_t=[1/(k_2Q_e^2)]+(t/Q_e)$	k_2/g·(mg·min)$^{-1}$ 0.2455		Q_e/mg·g^{-1} 555.5556	0.9999
	Intra-particle diffusion	$Q_t=k_{id}t^{0.5}+C$	K_{id1}/mg/(g·min$^{0.5}$) 4.2957		C_1/mg·g^{-1} 544.7405	0.9665
			K_{id2}/mg/(g·min$^{0.5}$) 0.3989		C_2/mg·g^{-1} 552.5580	
			K_{id3}/mg/(g·min$^{0.5}$) 0.0936		C_3/mg·g^{-1} 553.4740	0.9619
	Bangham	$\ln[1-(Q_t/Q_e]=-k_{fd}t$	α 0.0019		k_0 0.0371	
	Liquid film diffusion	$\log\{\log[C_0/(C_0-Q_t\cdot m)]\}$ $=\log(k_0m/2.303V)+\alpha\log t$	k_{fd} 0.1946			0.0757
	Elovich	$Q_t=(1/\beta)\ln(\alpha\beta)+(1/\beta)\ln t$	$\ln\alpha$ 512.8146		β/g·mg^{-1} 0.9304	0.6541
Thermodynamics	van't Hoff	$\ln K^{\Theta}=(-\Delta H/RT)+(\Delta S/R)$ $\Delta G=\Delta H-T\Delta S$	T/K	K^{Θ}	ΔH/kJ·mol^{-1}	ΔS/J·K^{-1}·mol^{-1}	ΔG/kJ·mol^{-1}	0.9999
			273.15	15.8690	11.2751	64.2614	−6.2779	
			278.15	17.3523	11.2751	64.2614	−6.5992	
			283.15	18.9125	11.2751	64.2614	−6.9205	
			288.15	20.5547	11.2751	64.2614	−7.2418	
			293.15	22.2724	11.2751	64.2614	−7.5631	
			298.15	24.0648	11.2751	64.2614	−7.8844	

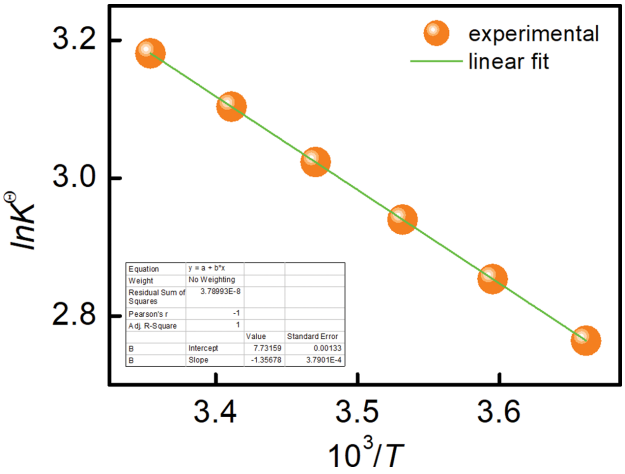


Fig. 18. Fitting curve of Cu(II) adsorption by GO based on van't Hoff equation.

determining step [27]. Furthermore, to unravel the characteristic steps involved in adsorption, fitting based on the IPD model was conducted, which gave a quite satisfactory result (Table 2). The IPD fitting curve (Fig. 17(d)) illuminates the three consecutive steps constituting adsorption: film diffusion, pore diffusion and surface complexation in sequence [28]. Clearly, surface complexation is the rate determining step as it has the smallest slope. Nonetheless, the fitting results of other kinetic models were unsatisfactory.

As Table 2 lists, thermodynamic functions are $\Delta G<0$, $\Delta H>0$, $\Delta S>0$, whereby spontaneous, endothermic and entropy increasing features are determined. Furthermore, ΔG becomes more negative with increasing temperature, manifesting the improvement of adsorption spontaneity. In the end, $\Delta S>0$ means the increase of system randomness due to adsorption.

3. Adsorption Mechanism

The adsorption affinity of the functional groups in GO towards Cu(II) can be evaluated from a quantitative aspect based on the

HSAB theory for a better understanding of the adsorption mechanism. To this end, the following two inequalities were summarized from Table 1 (|ΔE| denotes the absolute value of negative ΔE):

ΔN(Cu-COOH)<ΔN(Cu-OH)
|ΔE| (Cu-COOH)<ΔE(Cu-OH)

Above two inequalities disclose that more electrons were transferred, thus more energy was lowered concerning the interaction of OH with Cu(II) compared with that of COOH. This indicates that OH is stronger than COOH regarding binding affinity towards Cu(II).

FTIR, XPS spectra of the pre- and post-adsorption samples were measured to further explore the adsorption mechanism. Fig. 19 exhibits bands signifying SO_4^{2-} [29] appeared in the FTIR spectrum of $CuSO_4{\cdot}5H_2O$ at 1,066-865 cm^{-1}. While in the FTIR spectrum of the post adsorption sample, the corresponding bands appeared in 1,113-729 cm^{-1}. This noticeable band shift gives rise to two explorations: (1) Cu(Π) and SO_4^{2-} were adsorbed in pairs onto GO. (2) Interaction of SO_4^{2-} with GO is rather different from that with Cu^{2+} inside the $CuSO_4{\cdot}5H_2O$ crystal, which is mainly coulomb

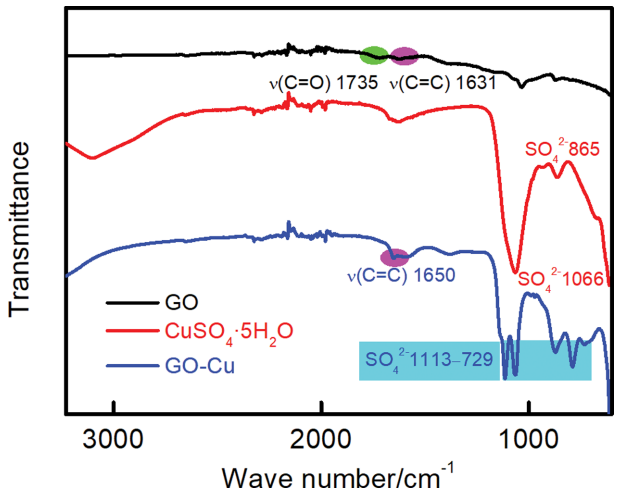


Fig. 19. FTIR spectra of GO, GO-$CuSO_4{\cdot}5H_2O$ (Cu(Π) origin) and GO-Cu (Cu(Π) loaded GO).

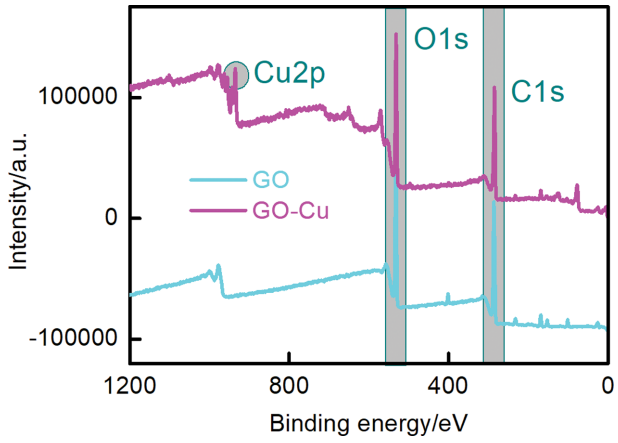


Fig. 20. XPS survey spectra of GO and GO-Cu (Cu(Π) loaded GO).

force. The C=O, C=C stretching vibrations in GO were detected at 1,735 cm^{-1}, 1,631 cm^{-1} [30], respectively. After adsorption, C=O band nearly vanished, and C=C band shifted to 1,650 cm^{-1}. These findings suggest the contribution of C=O, C=C related groups to adsorption [31].

Fig. 20 shows the XPS survey spectra, in which the C1s and O1s peaks stem from the intrinsic carbon and oxygen elements in GO [31]. The appearance of Cu2p peak [32] in the post adsorption sample verifies the successful attachment of Cu(Π). The high reso-

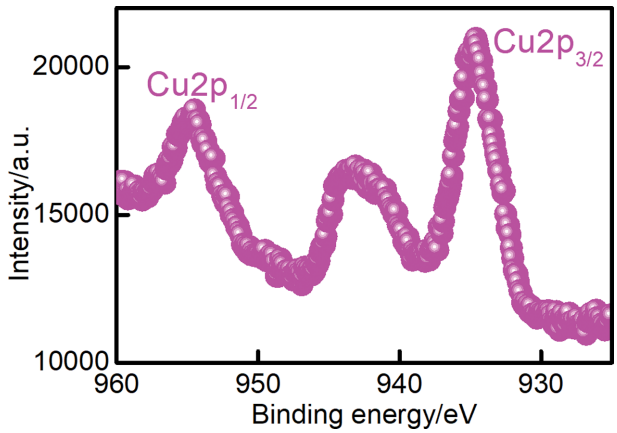


Fig. 21. Cu2p spectrum of GO-Cu (Cu(Π) loaded GO).

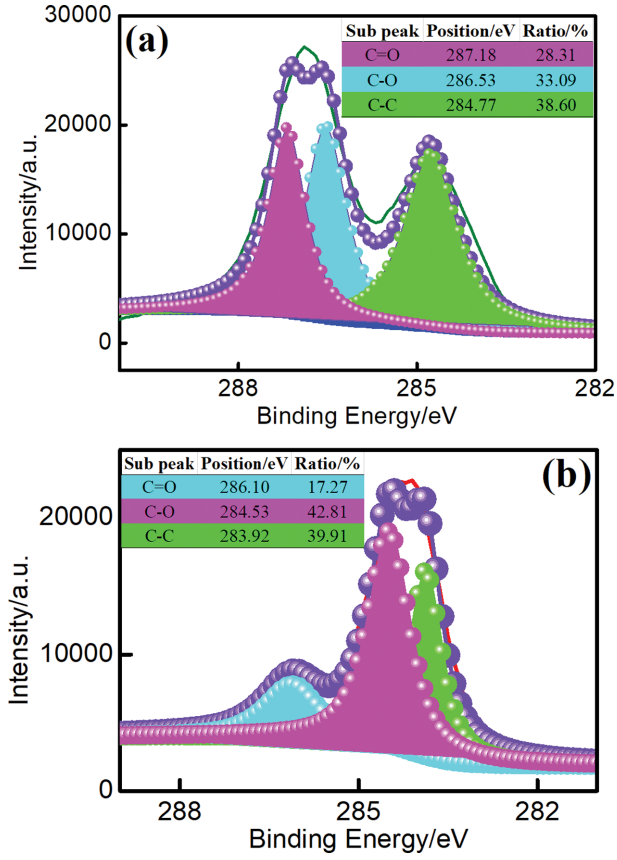


Fig. 22. High resolution C1s spectrum of (a) GO, (b) GO-Cu (Cu(Π) loaded GO).

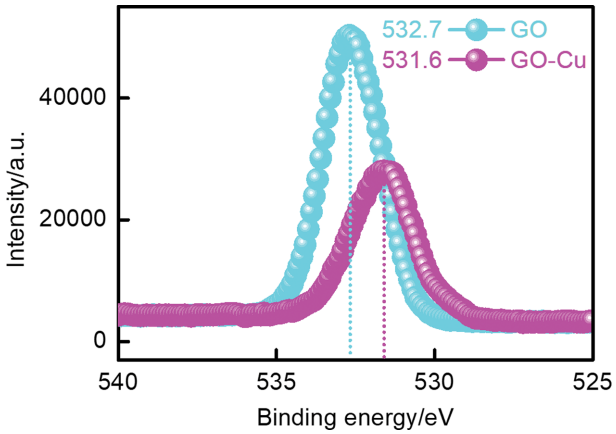
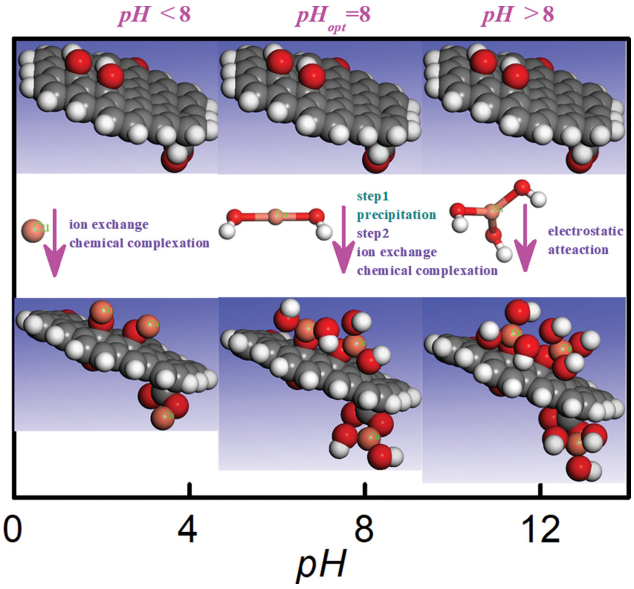


Fig. 23. O1s spectra of GO and GO-Cu (Cu(Π) loaded GO).



Scheme 1. Proposed adsorption mechanism of Cu(Π) by GO under different pH range. pH_{opt}=8 denotes the pH under which adsorption performance is optimized.

lution Cu2p peak is illustrated in Fig. 21. The C1s spectra was resolved into three sub peaks as C=O, C-O and C-C [32] to output the high resolution spectra via deconvolution, shown in Fig. 22. Careful inspection reveals three changes of the post adsorption sample compared with that of the pre adsorption one: (1) Change in position. The three sub peaks of GO redshifted from 287.18 eV, 286.53 eV, 284.77 eV to 286.10 eV, 284.53 eV, 283.92 eV, respectively, after adsorption. (2) Change in shape. The ratio of the three sub peaks C=O, C-O, C-C changed remarkably after adsorption, leading to the change in the peak shape as a whole. Especially, the change of C=O, C-O ratio was rather prominent as to change from 28.31%, 33.09% to 17.27%, 42.81%, indicating the contribution of C=O, C-O related groups such as carboxyl and hydroxyl to adsorption. (3) Change in intensity. The overall peak intensity decreased markedly after adsorption. Above three findings indicate that the chemical impact brought by Cu(Π) complexation is rather signifi-

Table 3. Description of the plausible adsorption mechanism of Cu(Π) by GO under different pH range

pH	Mechanism	Formula
<8	Ion exchange	$GO\text{-}COOH+Cu^{2+}\rightarrow GO\text{-}COO\text{-}Cu+H^{+}$
	Chemical complexation	$GO\text{-}OH+Cu^{2+}\rightarrow GO\text{-}O\text{-}Cu+H^{+}$
	Precipitation	$Cu^{2+}+2OH^{-}\rightarrow Cu(OH)_2\downarrow$
8	Ion exchange	$GO\text{-}COOH+Cu(OH)_2\rightarrow GO\text{-}COO\text{-}Cu(OH)_2+H^{+}$
	Chemical complexation	$GO\text{-}OH+Cu(OH)_2\rightarrow GO\text{-}O\text{-}Cu(OH)_2+H^{+}$
>8	Electrostatic attraction	$GO\text{-}COOH+Cu(OH)_3^{-}\rightarrow GO\text{-}COOH\text{-}Cu(OH)_3^{-}$
		$GO\text{-}OH+Cu(OH)_3^{-}\rightarrow GO\text{-}OH\text{-}Cu(OH)_3^{-}$

Table 4. Performance comparison of GO with reported results

Adsorbent	Adsorbate	D/mg·L^{-1}	C_0/mg·L^{-1}	te/min	Q_{max}/mg·g^{-1}	Ref.
Graphene oxide	Cu(II)	1,250	5-120		83.2	[21]
Graphene oxide/polyethyleneimine sponge	Cu(II)	1,250	5-120		150.9	[21]
Modified graphene oxide composite aerogels	Cu(II)	1,000	400	240	148.49	[30]
Graphene oxide/montmorillonite composite aerogel	Cu(II)		10-30		101.83	[32]
β-Cyclodextrin/magnetic graphene oxide/triethylenetetramine functionalized magnetically polyampholyte hydrogel	Cu(II)			90	140.50	[33]
Functionalized graphene oxide/carboxymethyl chitosan composite aerogels	Cu(II)		500		170.3	[34]
Functionalized graphene nanosheets	Cu(II)	1,000	30	60	28.80	[35]
Graphene oxide	Cu(II)	10	100	60	277.77	[36]
Carboxylated graphene oxide	Cu(II)	10	100	60	357.14	[36]
GO	**Cu(II)**	**500**	**300**	**12**	**553.90**	**this work**

cant. Fig. 23 compares the corresponding O1s spectra of the pre- and post-adsorption sample. Likely, two notable changes can be summarized: (1) Change in position. O1s peak of GO redshifted form 532.7 eV to 531.6 eV. (2) Change in intensity. The overall peak intensity decreased observably after adsorption. Above two explorations similarly suggest the remarkable chemical influence introduced by Cu(Π) complexation.

Finally, by combining all the above explorations regarding adsorption (which derived from pH effect on metal species, GO surface potential and adsorption efficiency, as well as HSAB theory, adsorption fittings, FTIR and XPS), the plausible adsorption mechanism was proposed, as tabulated in Table 3 and illustrated in Scheme 1.

4. Performance Evaluation

The adsorption performance of GO on Cu(Π) was compared with the reported results [21,30,32-36] of some similar adsorbents, which are summarized in Table 4. Clearly, GO has favorable adsorption capacity and rapid equilibration. These suggest that the graphene oxide prepared by the improved Hummers method has application potential for heavy metal scavenging.

CONCLUSION

An improved Hummers method was employed to prepare graphene oxide (GO). Adsorption efficiency of the as prepared GO towards aqueous Cu(II) was examined. More importantly, the "species resolved" adsorption mechanism was revealed via incorporating multiple evidence extracted from Cu(II) species distribution, GO surface potential, adsorption experiment and fitting, HSAB theory, FTIR and XPS. Accordingly, the "species resolved" adsorption mechanism was finalized as follows. (1) When pH<8, bare Cu^{2+} is the dominant metal species, which is adsorbed via ion exchange and chemical complexation. (2) When pH=8, $Cu(OH)_2$ is the dominant species, precipitation, ion exchange and chemical complexation are the adsorption mechanism. (3) When pH>8, $Cu(OH)_3^-$ is the dominant species, electrostatic attraction serves as the adsorption mechanism. Moreover, HSAB theory proves OH is stronger than COOH regarding binding affinity towards Cu(II). With respect to adsorption efficiency, GO has favorable adsorption capacity and rapid equilibration on Cu(II). Explorations of this work bring some novel insights into the interaction mechanism of graphene oxide with heavy metals. Thereby, these insights may provide guidance for developing high performance adsorbent based on graphene for heavy metal scavenging.

AUTHORS' CONTRIBUTION

Chaoke Bulin conceptualized the whole work and wrote the article. Ting Guo and Rongxiang Zheng supervised the experimental work. Ruichao Zhao, Bangwen Zhang and Fang Liu Validatied and approved the final manuscript.

FUNDING

This work was financially supported by the research project for universities, Inner Mongolia Autonomous Region, China (NJZY21392) and the key research project of Inner Mongolia Autonomous Region, China (2020ZD17).

NOMENCLATURE

- i : i=0, e, t, signifies the start, equilibrium and any moment t of adsorption, respectively, as in Eqs. (2)-(3).
- C_i : concentration of Cu(II) solution [$mg \cdot L^{-1}$]
- D : adsorbent dosage [$mg \cdot L^{-1}$]
- R_i : adsorption percent [%]
- Q_i : adsorption quantity [$mg \cdot g^{-1}$]
- V : volume of Cu(II) solution [mL]
- m : adsorbent mass [g]
- ΔN : electron transfer induced by adsorption
- ΔE : energy lowering induced by adsorption
- X_A : absolute electronegativity of acid or adsorbate
- X_B : absolute electronegativity of base or adsorbent
- η_A : absolute hardness of acid or adsorbate
- η_B : absolute hardness of base or adsorbent
- Q_{max} : monolayer adsorption capacity given by Langmuir fitting or theoretical maximum adsorption capacity given by D-R fitting [$mg \cdot g^{-1}$]
- K_L : Langmuir adsorption constant [$L \cdot mg^{-1}$]
- R_L : separation or equilibrium factor within the framework of Langmuir model
- K_F : Freundlich constant related to adsorption capacity
- n : Freundlich constants related to adsorption intensity
- R : gas constant [8.314 $J \cdot mol^{-1} \cdot K^{-1}$]
- T : absolute temperature [K]
- A_T : Temkin constant corresponds to the adsorption heat [$J \cdot mol^{-1}$]
- B_T : Temkin equilibrium binding constant relates to the maximum binding energy [$L \cdot g^{-1}$]
- E : mean free energy of adsorption within the framework of D-R model [$KJ \cdot mol^{-1}$]
- ε : Polanyi potential within the framework of D-R model
- β_{DR} : constant relates to E within the framework of D-R model [$mol^2 \cdot J^{-2}$]
- k_1 : pseudo-first-order rate constant [min^{-1}]
- k_2 : pseudo-second-order rate constant [$g \cdot mg^{-1} \cdot min^{-1}$]
- K_{id} : intra-particle diffusion rate constant [$mg \cdot g^{-1} \cdot min^{-0.5}$]
- C : constant related to the thickness of the boundary layer within the framework of intra-particle diffusion model [$mg \cdot g^{-1}$]
- k_0 : constant within the framework of Bangham model
- α : constant within the framework of Bangham model or initial adsorption rate within the framework of Elovich model [$mg \cdot g^{-1} \cdot s^{-1}$]
- $\beta_{Elovich}$: desorption constant within the framework of Elovich model [$g \cdot mg^{-1}$]
- K^{Θ} : adsorption equilibrium constant [$L \cdot g^{-1}$]
- ΔG : adsorption free energy change [$KJ \cdot mol^{-1}$]
- ΔH : adsorption enthalpy change [$KJ \cdot mol^{-1}$]
- ΔS : adsorption entropy change [$J \cdot K^{-1} \cdot mol^{-1}$]
- R^2 : correlation coefficient of adsorption fitting

REFERENCES

1. M. Verma, I. Lee, J. Oh, V. Kumar and H. Kim, *Chemosphere*, **287**,

132385 (2022).
2. P. Goyal, C. S. Tiwary and S. K. Misra, *J. Environ. Manage.*, **277**, 111469 (2021).
3. W. Z. Zeng, W. X. Guo, B. Li, Z. S. Wei, D. D. Dionysiou and R. Y. Xiao, *J. Hazard. Mater.*, **408**, 124868 (2021).
4. R. Cstro-Munoz, L. L. Gonzalez-Melgoza and O. Garcia-Depraect, *Chemosphere*, **270**, 129421 (2021).
5. D. Liu, Y. Yuan, Y. Q. Wei, H. Zhang, Y. X. Si and F. Zhang, *J. Environ. Sci.*, **116**, 4351 (2022).
6. Y. Gomravi, A. Karimi and H. Azimi, *Korean J. Chem. Eng.*, **38**, 1843 (2021).
7. P. Sherugar, M. Padaki, N. S. Naik, S. D. George and D. H. K. Murthy, *Chemosphere*, **287**, 132085 (2022).
8. T. T. Zhang, W. Wang, Y. L. Zhao, H. Y. Bai, T. Wen, S. C. Kang, G. S. Song, S. X. Song and S. Komarneni, *Chem. Eng. J.*, **420**, 127574 (2021).
9. W. Y. Gao, M. R. Razanajatovo, Y. Song, X. Zhao, Z. Y. Zhao, Q. M. Peng, T. F. Jiao, X. J. Liu and Q. R. Zhang, *Chem. Eng. J.*, **429**, 132599 (2022).
10. X. Z. Jia, M. Peydayesh, Q. Huang and R. Mezzenga, *Small*, **184**, 2105502 (2022).
11. W. Zhou, P. T. Wu, L. Zhang, D. L. Zhu, X. N. Zhao and Y. H. Cai, *J. Hazard. Mater.*, **421**, 126721 (2022).
12. J. Yan and R. Li, *Sci. Total Environ.*, **813**, 152604 (2022).
13. W. S. Hummers and R. E. Offeman, *J. Am. Chem. Soc.*, **80**, 1339 (1958).
14. H. T. Yu, B. W. Zhang, C. K. Bulin, R. H. Li and R. G. Xing, *Sci. Rep.*, **6**, 36143 (2016).
15. C. K. Bulin, B. W. Zhang, T. Guo, Z. Y. Ma, B. Li, Y. H. Zhang, R. G. Xing and X. Ge, *Res. Chem. Intermediate*, **47**, 3825 (2021).
16. T. Guo and C. K. Bulin, *J. Phys. Chem.*, **158**, 110251 (2021).
17. R. G. Pearson, *J. Am. Chem. Soc.*, **84**, 16 (1962).
18. R. G. Parr and R. G. Pearson, *J. Am. Chem. Soc.*, **105**, 7512 (1983).
19. R. G. Pearson, *J. Org. Chem.*, **27**, 734 (1988).
20. K. Gupta, S. R. Yasa, A. Khan, O. P. Sharma and O. P. Khatri, *J. Colloid Interface Sci.*, **607**, 1973 (2022).
21. Y. Kuang, Z. Y. Zhang and D. Y. Wu, *Sci. Total Environ.*, **806**, 151258 (2022).
22. S. Y. Xiong, Z. J. Wu and Z. L. Li, *Chemosphere*, **287**, 132418 (2022).
23. P. Joshi, O. P. Sharma, S. k. Ganguly, M. Srivastava and O. P. Khatri, *J. Colloid Interface Sci.*, **608**, 2870 (2022).
24. S. Singh, A. G. Anil, S. Khasnabis, V. Kumar, B. Nath, V. Adiga, T. S. S. K. Naik, S. Subramanian, V. Kumar, J. Singh and P. C. Ramamurthy, *Environ. Res.*, **203**, 111891 (2022).
25. P. Ammendola, F. Raganati and R. Chirone, *Chem. Eng. J.*, **322**, 302313 (2017).
26. S. Fan, Y. Wang, Z. Wang, J. Tang, J. Tang and X. D. Li, *J. Environ. Chem. Eng.*, **51**, 601611 (2017).
27. T. A. Saleh, A. Sa and M. Tuzen, *Chem. Eng. J.*, **307**, 230238 (2017).
28. M. A. Badawi, N. A. Negm, M. T. H. A. Kana, H. H. Hefni and M. M. A. Moneem, *Int. J. Biol. Macromol.*, **99**, 465476 (2017).
29. Y. Q. Zheng, B. Cheng, W. You, J. G. Yu and W. Ho, *J. Hazard. Mater.*, **369**, 214225 (2019).
30. Y. F. Zhang, L. Wu, H. L. Deng, N. Qiao, D. S. Zhang, H. Lin and Y. Y. Chen, *J. Environ. Chem. Eng.*, **9**, 106008 (2021).
31. S. Anuma, P. Mishra and B. R. Bhat, *J. Hazard. Mater.*, **416**, 125929 (2021).
32. X. Hao, S. Yang, T. E and Y. Li, *J. Hazard. Mater.*, **424**, 127680 (2022).
33. J. H. Yan and K. R. Li, *Sep. Purif. Technol.*, **277**, 119469 (2021).
34. J. Q. Luo, C. J. Fan and X. D. Zhou, *J. Appl. Polym. Sci.*, **138**, 50065 (2021).
35. M. L. Cao, Y. Li, H. Yin and S. Shen, *Ecotoxicol. Environ. Saf.*, **173**, 2836 (2019).
36. R. L. White, C. M. White, H. Turgut, A. Massoud and Z. R. Tian, *J. Taiwan Inst. Chem. Eng.*, **85**, 1828 (2018).